Journal of Applied Fluid Mechanics, Vol. 18, No. 6, pp. 1412-1429, 2025.
Available online at www.jafmonline.net, ISSN 1735-3572, EISSN 1735-3645.
https://doi.org/10.47176/jafm.18.6.3225

Numerical Investigation of the Aerodynamic and Aeroacoustic Characteristics of a Double-suction Centrifugal Fan under Different Operating Conditions

H. Zhang[1], J. W. Yang[2,3], S. G. Zhang[1], B. Li[3,4], J. Wei[3,4] and Y. F. Zhang[1†]

[1] *School of Aerospace Engineering, Tsinghua University, Beijing, 100084, China*
[2] *Healthy & Intelligent Kitchen Engineering Research Center of Zhejiang Province, Ningbo, 315336, China*
[3] *Ningbo Fotile Kitchen Ware Company, Ningbo, 315336, China*
[4] *Key Laboratory of Healthy & Intelligent Kitchen System Integration of Zhejiang Province, Ningbo, 315336, China*

†*Corresponding Author Email: zhangyufei@tsinghua.edu.cn*

ABSTRACT

Centrifugal fans are widely used in the ventilation and domestic appliance industries. Their aerodynamic and aeroacoustic characteristics vary significantly in different application scenarios and operating conditions. This study applied a double-suction multiblade centrifugal fan to a range hood. The full three-dimensional flow and acoustic field were calculated synchronously using direct computational aeroacoustics (CAA) based on the lattice Boltzmann method (LBM) to investigate the internal flow, aerodynamic noise, and acoustic source characteristics of the fan under different operating conditions. We focused on two typical operating conditions: the maximum volume flow rate and working volume flow rate. The accuracy of the numerical simulation was verified using experimental data measured from the performance test bench and the semianechoic chamber. The flow field results show that more than 70% of the airflow enters the volute from the main wind inlet; this asymmetric wind intake condition creates an asymmetric flow pattern inside the volute. Acoustic waves radiate to the far-field mainly through the inlet and outlet of the range hood. The propagation characteristics of a dipole source are not very obvious and the tonal noise associated with the blade passage frequency (BPF) is not significant. In addition to the acoustic sources identified in the impeller region, the volute tongue, and the gap between the impeller and the inlet nozzle, two other significant acoustic sources are identified in the outlet collector and inlet nozzle regions.

Article History

Received October 27, 2024
Revised December 9, 2024
Accepted January 20, 2025
Available online March 30, 2025

Keywords:

Centrifugal fan
Aerodynamic performance
Computational aeroacoustics
Acoustic source localization
Lattice Boltzmann method

1. INTRODUCTION

Double-suction multiblade centrifugal fans are widely used in industrial and civil applications because of their advantages of compact size, large flow rate, and high pressure, realizing significant economic and social benefits (Seo et al., 2003; Zhou et al., 2023). For example, the centrifugal fan is a core component of industrial ventilation systems, air conditioners, and range hoods. However, a fan's aerodynamic and aeroacoustic characteristics vary significantly in different application scenarios and operating conditions. Additionally, the rising prominence of the concepts of green, low-carbon technology and sustainable development are increasing expectations for high energy efficiency and improved quality of life (Basner et al., 2015). This has led to increased demands for better aerodynamic performance and noise management. It is therefore valuable to comprehensively investigate the aerodynamic and aeroacoustic characteristics of double-suction multiblade centrifugal fans under different operating conditions in actual application scenarios, with the aim of providing a foundational basis for designing high-efficiency and low-noise fans.

Computational fluid dynamics (CFD) and computational aeroacoustics (CAA) have been widely used in recent years to analyze the aerodynamics and aeroacoustics of multiblade centrifugal fans, particularly in cases where experimental research is difficult and costly. Numerous researchers have conducted extensive research on aerodynamic characteristics. Ye et al. (2018) and Wang et al. (2020) investigated the effects of blade

NOMENCLATURE

CFD	Computational Fluid Dynamics	Q_v	volume flow rate
CAA	Computational Aeroacoustics	P_s	outlet static pressure
LBM	Lattice Boltzmann Method	P_t	outlet total pressure
VLES	Very Large Eddy Simulation	η_t	total pressure efficiency
BPF	Blade Passage Frequency	n	motor rotation speed
FFT	Fast Fourier Transform	T_n	impeller torque
SPL	Sound Pressure Level	dp/dt	time derivative of pressure
OASPL	Overall Sound Pressure Level	V	velocity magnitude
TKE	Turbulence Kinetic Energy	V_y	y-velocity
AI	Articulation Index	V_r	radial velocity
SAM	Sound Absorption Material	f	frequency

trimming on fan aerodynamic performance and related flow mechanisms, finding that blade trimming with appropriate parameters enables higher fan aerodynamic performance in terms of total pressure efficiency and static pressure rise. Keyur and Prajesh (2013) and Bai et al. (2024) demonstrated that a reasonable readjustment of the blade inlet and outlet angles can significantly improve a fan's flow rate and efficiency. Gholamian et al. (2013) reported that a fan with an inlet nozzle almost equal in size to the internal impeller diameter exhibited the best efficiency and performance. Liu et al. (2021) designed a D-type inlet nozzle to suppress reverse flow and verified its performance improvement under low-flow conditions. Baloni et al. (2015) employed the Taguchi method to optimize the volute and enhance the centrifugal fan's performance. Wei et al. (2022) reported that the reasonable clearance ratio and inclined design of the volute tongue are beneficial for improving the flow pattern around the centrifugal fan's volute tongue and volute outlet and reducing the local flow loss. Their work evaluated the effects of components such as the impeller, inlet nozzle, and volute casing on the centrifugal fan's aerodynamic characteristics. Aerodynamic performance is improved by optimizing the component structure and aerodynamic matching between the components.

Aeroacoustics assessment is another significant consideration in the design of high-efficiency and low-noise fans. However, compared with evaluating aerodynamic performance, aeroacoustic prediction is a difficult CFD problem; the sound energy is much lower than the flow energy, posing a significant challenge for numerical methods and turbulence models (Zhang et al., 2022). There are currently two main methods used to predict aerodynamic noise: hybrid CAA and direct CAA. The former calculates the acoustic sources and propagation separately, whereas the latter calculates them synchronously. Although the Reynolds-averaged Navier–Stokes (RANS) approach can reasonably reveal the flow patterns inside a fan, it is unsuitable for CAA, which requires accurate schemes to capture the dynamics of acoustic fluctuations (Simon et al., 2009; Rui et al., 2020). For hybrid CAAs, researchers commonly use large eddy simulation (LES), detached-eddy simulation (DES), and unsteady RANS (URANS) methods to obtain the acoustic source and use the Ffowcs Williams and Hawkings (FW–H) equation to calculate the far-field noise (Lu et al., 2023). However, only the LES method can provide multiscale noise sources that yield broadband noise (Carlos et al., 2019). Kim et al. (2015) evaluated the internal flow and noise of a multiblade centrifugal fan using the LES/FW–H method, noting that the effects of turbulence noise caused by the disturbance and dissipation of eddies are not reflected because the quadrupole acoustic source is disregarded. Using the same method, Chen et al. (2018) revealed that the pressure fluctuations on the volute surfaces, especially on the tongue surface, are the main dipole source. While being known for its high efficiency, the hybrid method inevitably disregards the quadrupole acoustic source. In addition, the selection strategy for the integration surface remains unclear for complex configurations containing sound absorption materials in actual application scenarios. Direct CAA represents a more general approach to revealing the fundamental mechanism of aerodynamic noise generation.

Theoretically, the acoustic source and propagation can be obtained simultaneously by directly solving the compressible N–S equations. However, this requires substantial computational resources, making it infeasible in engineering practice (Tim & Sanjiva, 2004). The lattice Boltzmann method (LBM) on a Cartesian grid has emerged in recent years as an excellent candidate to address noise problems in realistic complex geometries (Moreau, 2022). Unlike traditional implementations of macroscopic conservation equations, the LBM always solves the unsteady flow field via relatively small time steps, enabling accurate resolution of the fluctuating pressures responsible for acoustics (Rebecca & Martin, 2020). Additionally, the LBM scheme has low numerical dissipation, resulting in acoustic waves that can propagate accurately from the flow region and flow-induced noise sources to the far field (Melanie et al., 2014). Based on the direct CAA of the LBM, Stephan et al. (2013) successfully investigated the effect of a flow control obstruction at the fan inlet on the aerodynamic performance and noise of multiblade centrifugal fans. Rebecca and Martin (2019) performed direct noise computations on the aerodynamics and aeroacoustics of centrifugal fans using the LBM, demonstrating that the best result in terms of accuracy and computational effort can be obtained with a mesh size of 0.4 mm for the donut-like ring refinement of the impeller. Similarly, this method has also been used to successfully predict the aerodynamic noise problems of helicopters (Gianluca & Damiano, 2019), electrically propelled vertical take-off and landing (eVTOL) vehicles (Casalino et al., 2019), aerofoil (Gianluca et al., 2021), landing gear (Michael et al., 2021), and turbofans (Damiano et al., 2019). In addition, Kazuya et al. (2020) assessed the computational accuracy and speed of the LBM using a

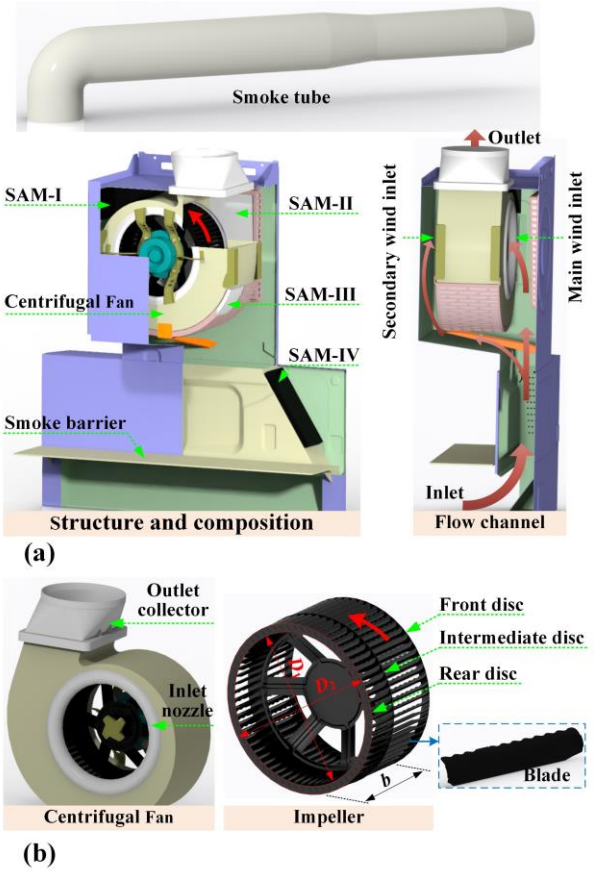

Fig. 1 Geometric model: (a) Range hood and (b) double-suction multiblade centrifugal fan

pulse-propagating problem. The results indicate that the computational speed of the LBM is 12.3 times faster than that of the compressible N–S equation. The above studies demonstrate the efficiency of the LBM as a computational method for aeroacoustic simulations.

Although valuable advances have been made in the numerical simulation of aerodynamic and aeroacoustic characteristics, most of the fans reported in the above literature were operated alone in an open wind intake environment. More physical insight into the aerodynamic and aeroacoustic characteristics of fans in actual application scenarios is needed. More importantly, the acoustic source location must be identified to guide noise reduction design. This study therefore considered the application scenario of a double-suction multiblade centrifugal fan in a range hood. We conducted an accurate numerical study of the unsteady flow and acoustic field from the range hood using a full-scale geometric model via the direct CAA method based on the LBM. We investigated two typical operating conditions in accordance with the actual operation of the range hood: the maximum volume flow rate and the working volume flow rate. Experimental data from the performance test bench and the semianechoic chamber were used to validate the accuracy of the numerical simulation results. The calculation strategies used and the acoustic sources identified provide useful references for the design of high-efficiency and low-noise fans.

Table 1 Basic parameters of the centrifugal fan

Parameters	Value
Number of blades, Z	63
Impeller inner diameter, D_1 (mm)	230
Impeller outer diameter, D_2 (mm)	263
Impeller width, b (mm)	145
Blade inlet angle, β_{1A} (°)	76
Blade outlet angle, β_{2A} (°)	173
Blade thickness, δ (mm)	0.4

2. MATERIALS AND METHODS

2.1 Geometric Model

The double-suction multiblade centrifugal fan investigated in this study was applied to a domestic appliance range hood. Since aerodynamic noise calculations are sensitive to geometrically small structures, a full-scale geometric model was used for numerical simulations. Figure 1 illustrates the geometric structure and composition of the range hood, which includes a centrifugal fan, an outlet collector, a shell, a smoke collection channel, some sound absorption materials (SAM), a smoke tube, and some fixed parts. The materials SAM-I and SAM-IV are polyurethane (PU), while the materials SAM-II and SAM-III are synthesized from polypropylene (PP) and polyethylene terephthalate (PET), respectively. The centrifugal fan comprises an impeller, a volute, two inlet nozzles, and a motor. The airflow originates from below, first passing through a narrow smoke collection channel, then through the front and rear intake chambers, and finally passing through the corresponding inlet nozzles into the fan. The centrifugal fan's inlets in the front and rear intake chambers are referred to as the secondary wind inlet and the main wind inlet, respectively. The impeller rotates counterclockwise and consists of 63 forward-curved single arc blades with a wavy trailing edge and equal thickness. The front disc is near the main wind inlet, followed by the intermediate disc and the rear disc. The detailed structural parameters of the fan are presented in Table 1.

The operating conditions of the range hood match the actual emission requirements of the lampblack. This study investigated the aerodynamic and noise characteristics of a range hood under two operating conditions: the maximum volume flow rate (Case 1) and the working volume flow rate (Case 2). These are two typical conditions that both manufacturers and consumers focus on. With respect to Case 1, although the maximum volume flow rate can effectively meet the emission requirements of large quantities of instantaneous lampblack, it results in the highest noise level. For Case 2, the actual working scenario was simulated by installing a smoke tube on the outlet collector, which is the range hood's operating condition over a long period of time. Table 2 shows the detailed performance parameters of the range hood under different operating conditions, including the volume flow rate Q_v, motor rotation speed n, outlet static pressure $P_{s,}$ and total pressure efficiency η_t.

Table 2 Performance parameters of the range hood under two typical operating conditions

Parameters	Case 1	Case 2
Q_v (m^3/min)	24.17	10.24
n (rpm)	1054	1300
P_s (Pa)	0.0	342.88
η_t (%)	22.51	40.53
Smoke tube	Not included	Included

2.2 Governing Equations and Turbulence Model

The range hood's unsteady flow and radiated acoustics were determined using the fully explicit, transient, compressible lattice Boltzmann (LB) equation implemented in the solver SIMULIA PowerFLOW. It is based on the principle of performing very large eddy simulations (VLES) to simulate resolvable flow scales while modeling unresolved scales by modifying the relaxation time computed from a renormalization group (RNG) k-ε model underlying simulation. This approach is referred to as the very large eddy simulation based on the lattice Boltzmann method (LBM–VLES). Unlike conventional numerical schemes based on the discretization of macroscopic continuum equations, the LBM is based on microscopic models and mesoscopic kinetic equations and is used to predict the macroscopic behavior of the flow (Rebecca & Martin, 2020).

The LB equation is a kinetic equation describing the streaming and collision of particles with a finite number of velocities (Chen & Doolen, 1998). As shown in Fig. 2, the Cartesian space is spatially discretized into an equidistant mesh, and each mesh cell is referred to as a lattice. In addition, the velocity is discretized to predefined velocity directions in the three-dimensional case. For these discrete velocity vectors, one particle is advected from one point of the mesh to 19 adjacent points within a prescribed time step, including the point itself (D3Q19, namely, three dimensions and 19 velocity states) (Rebecca & Martin, 2019).

In addition, the calculations associated with the collision term in the original nonlinear LB equation involve a complex integral requiring excessive storage and computational resources. Therefore, the collision term can be modeled with the well-known Bhatnagar–Gross–Krook (BGK) approximation (Gianluca et al., 2021). The discrete BGK–Boltzmann equation presented in Eq. (1) is referred to as the lattice-BGK (LBGK) equation and can be used to effectively reduce the computational cost.

$$f_i(\mathbf{X}+\mathbf{V}_i\Delta t, t+\Delta t) - f_i(\mathbf{X},t) = -\frac{\Delta t}{\tau}\left[f_i(\mathbf{X},t) - f_i^{eq}(\mathbf{X},t)\right] \quad (1)$$

In this equation, f_i is the distribution function of a particle with velocity $\mathbf{V}_i$ at position $\mathbf{X}$ and time t along the ith direction, according to the finite set of discrete velocities ($\mathbf{V}_i$: i = 0, 1, …, 19), and $\Delta\mathbf{X} = \mathbf{V}_i\,\Delta t$, where $\Delta\mathbf{X}$ and Δt are the space increment and time increment, respectively. The left-hand side of Eq. (1) represents the convective motion of the particles (i.e., streaming). The right-hand side expresses complex intermolecular interactions (i.e., collision operators), assuming that the particles relax to

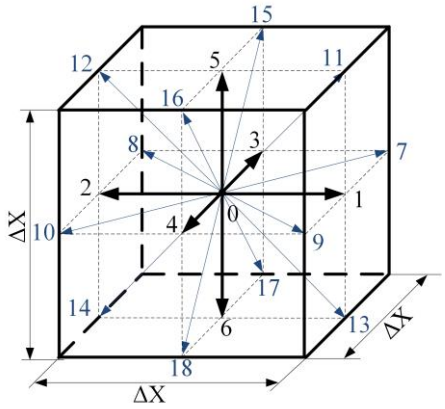

Fig. 2 Schematic of the D3Q19 lattice

the local equilibrium states represented by f_i^{eq} at relaxation time τ. By using the Taylor series expansion of the Maxwell–Boltzmann distribution function with fluid velocity $\mathbf{u}$ up to second order for low Mach numbers, the equilibrium distribution function f_i^{eq} is obtained as follows (Qian et al., 1992; Kazuya et al., 2020):

$$f_i^{eq} = \rho w_i\left[1 + \frac{\mathbf{V}_i\mathbf{u}}{c_s^2} + \frac{(\mathbf{V}_i\mathbf{u})^2 - (c_s|\mathbf{u}|)^2}{2c_s^4}\right] \quad (2)$$

where the constant sound speed $c_s = 1/\sqrt{3}$ and the weight coefficients are written as

$$w_i = \begin{cases} 1/18 & i = 1,\ldots,6 \\ 1/36 & i = 7,\ldots,18 \\ 1/3 & i = 0 \end{cases} \quad (3)$$

The macroscopic density ρ (kg/m^3), velocity $\mathbf{u}$ (m/s), and pressure p (Pa) are computed as

$$\rho = \sum_i f_i \quad (4)$$

$$\rho\mathbf{u} = \sum_i \mathbf{V}_i f_i \quad (5)$$

$$p = \rho c_s^2 \quad (6)$$

To model the turbulent fluctuations, the small and unresolved flow scales are represented by replacing the molecular relaxation time τ with an effective turbulent relaxation time τ_{eff}, which can be expressed as (Chen et al., 2003)

$$\tau_{eff} = \tau + C_\mu \frac{k^2/\varepsilon}{T\left(1+\eta^2\right)^{1/2}} \quad (7)$$

where C_μ = 0.085; T is the absolute temperature; and $\tilde{\eta}$ is a function of the local strain parameter $\eta_s = k|\mathbf{S}|/\varepsilon$, local vorticity $\eta_\omega = k|\mathbf{\Omega}|/\varepsilon$ parameter, and local helicity $\eta_h = k(|\mathbf{u}\cdot\mathbf{\Omega}|/|\mathbf{u}|)/\varepsilon$ parameter. The turbulent kinetic energy k and the turbulent dissipation ε are determined according to the RNG k-ε equations. In addition, a wall function approach is used to model boundary layers on solid surfaces.

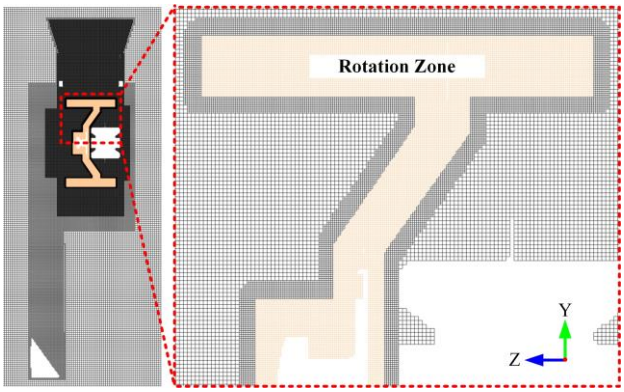

Fig. 3 Schematic of the computational domain and mesh configuration

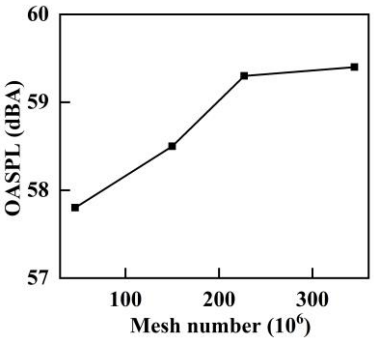

Fig. 4 Mesh independence

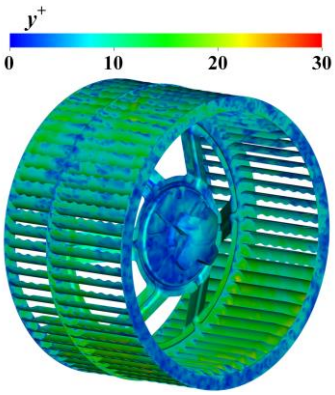

Fig. 5 Distribution of *y*+ on the surface of blades

The sound absorption material is defined via an acoustic porous medium governed by Darcy's law. Further details are provided by Freed (1998) and Teruna et al. (2020). Therefore, in this work, we determined the parameters used to simulate the acoustic properties of real sound absorption materials on the basis of the sound absorption coefficient.

2.3 Computational Domain and Mesh Configuration

The LBM–VLES scheme was solved on a Cartesian mesh composed of cubic volumetric elements. The dimensions of the computational domain are consistent with those of a semianechoic chamber. The floor was defined as a wall, and the other boundary conditions were pressure outlets (absolute pressure of 101325 Pa). Similar to the approach used by Rebecca and Martin (2020), we modeled the foam on the ceiling and surrounding walls as a high-viscosity region to absorb sound waves and prevent the effect of sound wave reflections on the sound field around the range hood.

As shown in Fig. 3, the same mesh configuration was used in both cases, increasing the volume discretization in regions of interest or where high flow gradients are expected. The mesh size is the smallest in the rotation zone of the impeller and gradually increases toward the outside. A sliding mesh approach was used to model the impeller's rotation according to the measured average rotation speed presented in Table 2. The boundary of the rotation zone was thus offset toward the adjacent stationary zone, and the smallest mesh size was also adopted to ensure stable data transmission between the two zones. Mesh independence was critically evaluated to ensure numerical accuracy. The overall sound pressure level (OASPL) of the range hood for different mesh numbers is demonstrated in Fig. 4. The OASPL was calculated as described in Sec. 2.4. The fine mesh was used for all simulations. At this moment, the minimum mesh size in the rotation zone of the impeller is $\Delta x = 0.382$ mm.

In the zone where the microphone observation points are located, the mesh size is 6.12 mm. According to Guillaume et al. (2009), at least 12–16 mesh points per wavelength should be adopted for the propagation of acoustic waves. This study focused on a maximum frequency of 4000 Hz (corresponding to a wavelength of 85 mm), meaning that there are approximately 14 grid points per wavelength with reasonable numerical truncations. There are 110 million meshes in the rotation zone and 345 million meshes in total.

The impeller, as the sole moving component, exhibits the most complex flow patterns within the rotation zone. Figure 5 shows the distribution of *y*+ on the blades' surfaces as an indicator of the size of the first-layer grid. The value of *y*+ is generally less than 20 across the majority of the blade surface and does not exceed a maximum of 30.

High-frequency pressure fluctuations can also be captured to assess fan noise levels when the impeller rotation angle is less than 0.5° per time step (Yang et al., 2024). In this study, the computational time step $\Delta t = 1.808\times10^{-6}$ s, meaning that the impeller rotation does not exceed 0.1° per time step, which meets noise numerical simulation requirements.

2.4 Direct CAA for Noise Prediction

The full three-dimensional flow and acoustic field were calculated synchronously via direct CAA based on the LBM. This means that the noise level of the microphone observation points can be evaluated based on the pressure fluctuations recorded at that point within the fluid domain. The time signals were transferred to the frequency range via a fast Fourier transform (FFT) with a Hanning window and then converted to sound pressure levels (SPLs) using a reference sound pressure of 2×10^{-5} Pa (Eq. 8). A-weighting of the SPL was employed (Eq. 9), considering the perceptual characteristics of the human

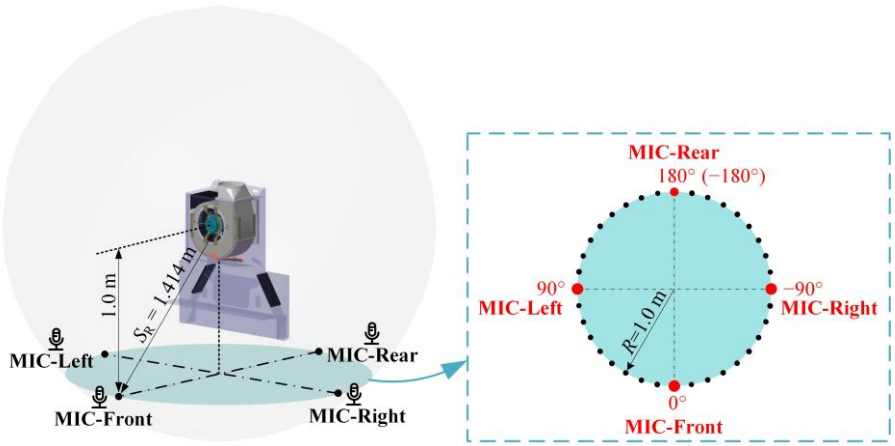

Fig. 6 Locations of microphone observation points based on the global envelope method

auditory system in response to different sound wave frequencies. The aeroacoustic characteristics of the microphone observation points were determined using the OASPL obtained from the frequency analysis (Eq. 10) (Rebecca & Martin, 2020):

$$L_{p,ij} = 20\log_{10}\left(\frac{p_{rms,ij}}{p_{ref}}\right) \tag{8}$$

$$L_{p,ij}(\mathrm{A}) = L_{p,ij} - 20\log_{10}\left(\frac{1.258897(12200\, f_{ij}^2)^2}{(f_{ij}^2+20.6^2)(f_{ij}^2+12200^2)\sqrt{(f_{ij}^2+107.7^2)(f_{ij}^2+737.9^2)}}\right) \tag{9}$$

$$L_{p,i}(\mathrm{OA}) = 10\log_{10}\left(\sum_{j=1}^{n_j} 10^{0.1L_{p,ij}(\mathrm{A})}\right) \tag{10}$$

where $L_{p,ij}$ is the SPL at microphone observation point i and frequency band j (dB); $p_{rms,ij}$ is the root mean square of pressure, also known as sound pressure (Pa); p_{ref} is the reference sound pressure (Pa); $L_{p,ij}$(A) is the A-weighting of the sound pressure level (dB(A)); f_{ij} is the frequency (Hz); $L_{p,i}$(OA) represents the OASPL at microphone observation point i (dB(A)); and n_j is the number of frequency bands.

As Fig. 6 shows, microphone observation points were selected on a spherical surface with a radius of 1.414 m on the basis of the global envelope method. These points are uniformly distributed on the circumference formed by the intersection of a horizontal plane 1.0 m below the center of the impeller and the spherical surface. The interval between two adjacent observation points is 10°. The range hood's noise level was assessed using the average OASPL $L_{p,ave}$(OA) of the following four observation points: MIC-Front, MIC-Rear, MIC-Left, and MIC-Right (Eq. 11).

$$L_{p,ave}(\mathrm{OA}) = \frac{1}{4}\sum_i L_{p,i}(\mathrm{OA}) \tag{11}$$

2.5 Experimental Measurements

Figure 7 illustrates the test sites for the aerodynamic and aeroacoustic characteristic measurements. The aerodynamic performance test was conducted within the test chamber, which was maintained at an ambient temperature of 20 ± 5 °C, a relative humidity of less than 85%, and with an absence of external airflow and thermal

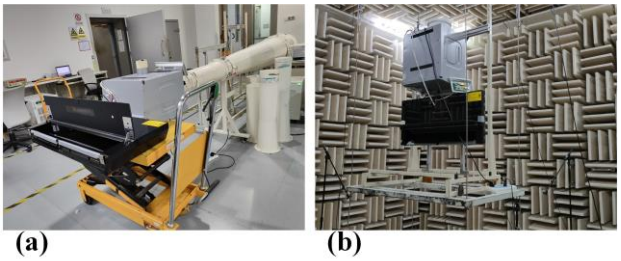

Fig. 7 Experimental measurements: (a) Aerodynamic performance test bench and (b) semianechoic chamber

radiation. The outlet collector of the range hood under testing was sealed to the test bench via a connector during the measurements to ensure no air leakage under any operating conditions. The fan was operated under typical conditions by adjusting the hole board throttling device. The airflow from the range hood's outlet collector passed through a cross-rectifier and a diffuser, ensuring uniform flow over the unit rectifier. The static pressure Δp at the throttling orifice plate was calculated by averaging the four evenly distributed pressure taps. The remaining aerodynamic parameters were determined by the following equations (Liu et al., 2021):

$$Q_v = 1.111\times\alpha d^2\times\sqrt{\frac{\Delta p}{\rho}} \tag{12}$$

$$P_t = \Delta p + 0.5k_0\left(\frac{Q_v}{A}\right)^2 \tag{13}$$

$$P_s = P_t - 0.5\rho\left(\frac{Q_v}{A}\right)^2 \tag{14}$$

$$\eta_t = \frac{Q_v\times P_t}{W_{input}}\times 100\% \tag{15}$$

where α and d represent the coefficient and diameter of the hole board throttling device, respectively; ρ is the air density; k_0 is the area ratio between different sections of the measuring pipe; A represents the area of the fan outlet; and η_t is the total pressure efficiency. The motor efficiency

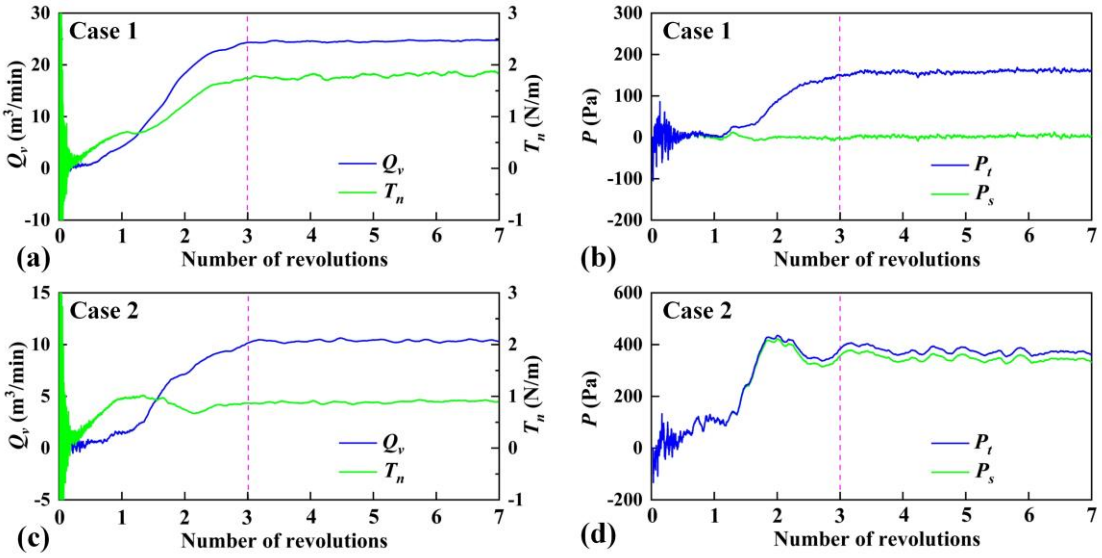

Fig. 8 Time history of the aerodynamic performance parameters: (a) Volume flow rate Q_v and impeller torque T_n for Case 1, (b) total pressure P_t and static pressure P_s for Case 1, (c) volume flow rate Q_v and impeller torque T_n for Case 2, and (d) total pressure P_t and static pressure P_s for Case 2

was removed from the total pressure efficiency derived from the CFD simulations.

The range hood was suspended in the center of the semianechoic chamber, with a distance between its lowest part and the floor of at least 1.3 m. The wind inlet and outlet were situated in an area of free space and operated continuously for 30 minutes before measurements commenced. The acoustic signals were monitored by microphones placed at four observation points. The resulting experimental data were compared with the simulated data.

3. RESULTS AND DISCUSSION

3.1 Validation of the Numerical Simulation

For both operating cases, the simulations were performed over seven impeller revolutions. The corresponding computational costs were 1657 CPU hours per revolution and 1342 CPU hours per revolution, respectively. All simulations were conducted on a high-performance cluster.

To check the convergence of the simulation, the parameters (volume flow rate Q_v, total pressure P_t, and static pressure P_s) at the fan outlet and the impeller torque T_n were monitored on the basis of a time series over the seven revolutions. As shown in Fig. 8, the parameters (Q_v, P_t, P_s, and T_n) reach a stable state after three revolutions, indicating that the simulation has converged. The strong, unsteady effect of the flow inevitably leads to small amplitude fluctuations. Therefore, we used the average value of the data from the last four revolutions to evaluate the fan's aerodynamic performance. Figure 9 presents a comparison of the experimental and simulation results of the aerodynamic performance parameters. At the same outlet static pressure, the relative errors of Q_v for Case 1 and Case 2 are 1.55% and 0.68%, respectively; the differences in ηt are 3.57% and 2.09%, respectively. Small differences between the simulation and the experiment results can be attributed to the unstable rotation speed of the experimental motor. Therefore, current simulations can represent the range hood's expected typical operating conditions and prove that the numerical simulation method is accurate and can effectively model the fan's aerodynamic characteristics.

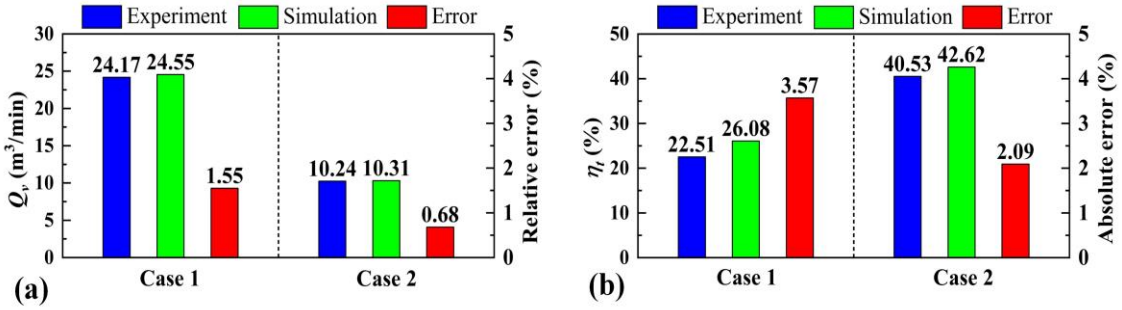

Fig. 9 Comparison of experimental and simulation results of aerodynamic performance parameters: (a) Volume flow rate Q_v and (b) total pressure efficiency η_t

Table 3 Comparison of experimental and simulation results for the OASPLs at the microphone observation points

	OASPL (dBA)	MIC-Front	MIC-Rear	MIC-Left	MIC-Right	Average
Case 1	Simulation	63.3	56.8	58.2	59.2	59.4
	Experiment	62.1	56.7	58.0	57.9	58.7
	Absolute error	1.2	0.1	0.2	1.3	**0.7**
Case 2	Simulation	58.7	52.1	52.0	53.8	54.2
	Experiment	57.3	52.0	51.6	52.9	53.5
	Absolute error	1.4	0.1	0.4	0.9	**0.7**

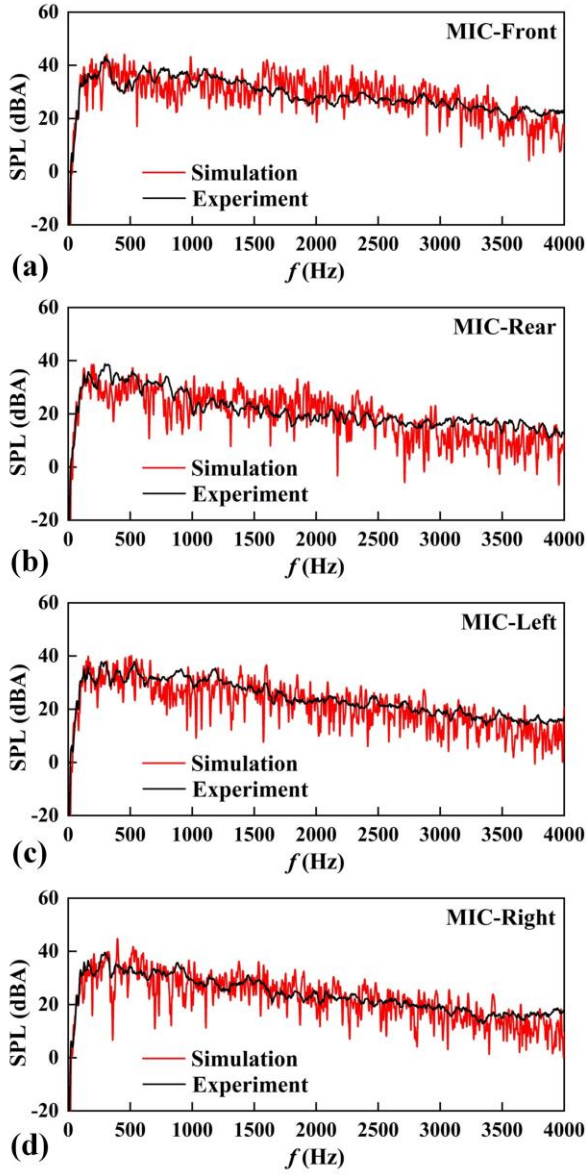

Fig. 10 Spectra of the SPL at the microphone observation points for Case 1

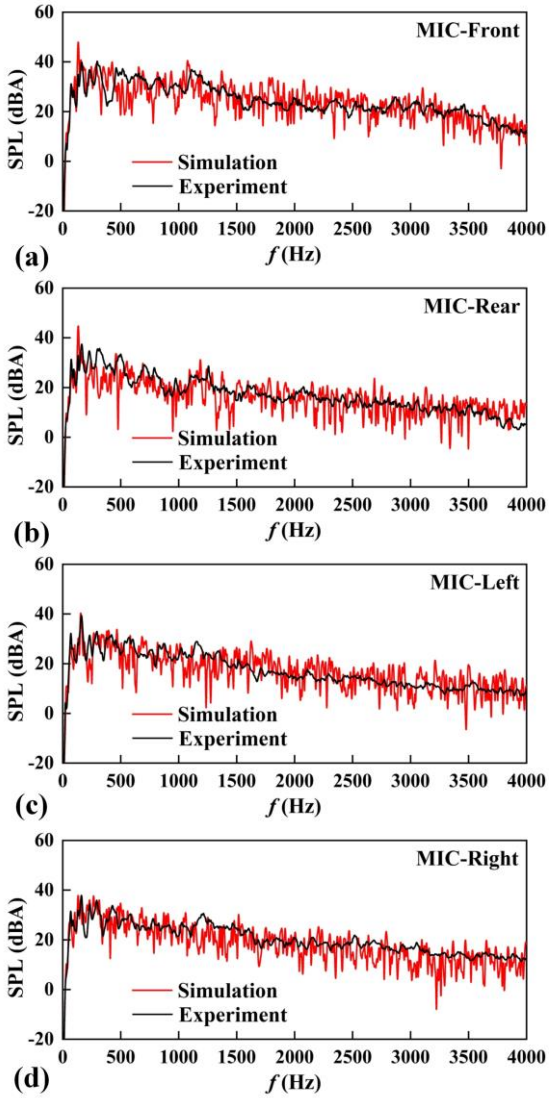

Fig. 11 Spectra of the SPL at the microphone observation points for Case 2

Figures 10 and 11 present comparisons of the spectra for the SPL at the microphone observation points obtained from the numerical simulation and experimental measurements for Case 1 and Case 2, respectively. The corresponding blade passage frequencies (BPFs) are 1106.7 Hz and 1365 Hz. Although some humps cannot be predicted at exactly the same frequency, the simulation captures the same acoustic features of the measurements.

For both cases, the simulations capture the broadband noise well and maintain the same trend as that of the measurements. Over the frequency range of interest (0~4000 Hz), there are no significant differences between the high-frequency bands of the simulated values and those of the experimental values. This finding indicates that the currently used mesh size is sufficient for resolving the strong pressure fluctuation areas to achieve a direct aerodynamic noise simulation of the range hood.

Additionally, the predicted OASPLs are accurate for both cases. Table 3 shows the experimental and simulation

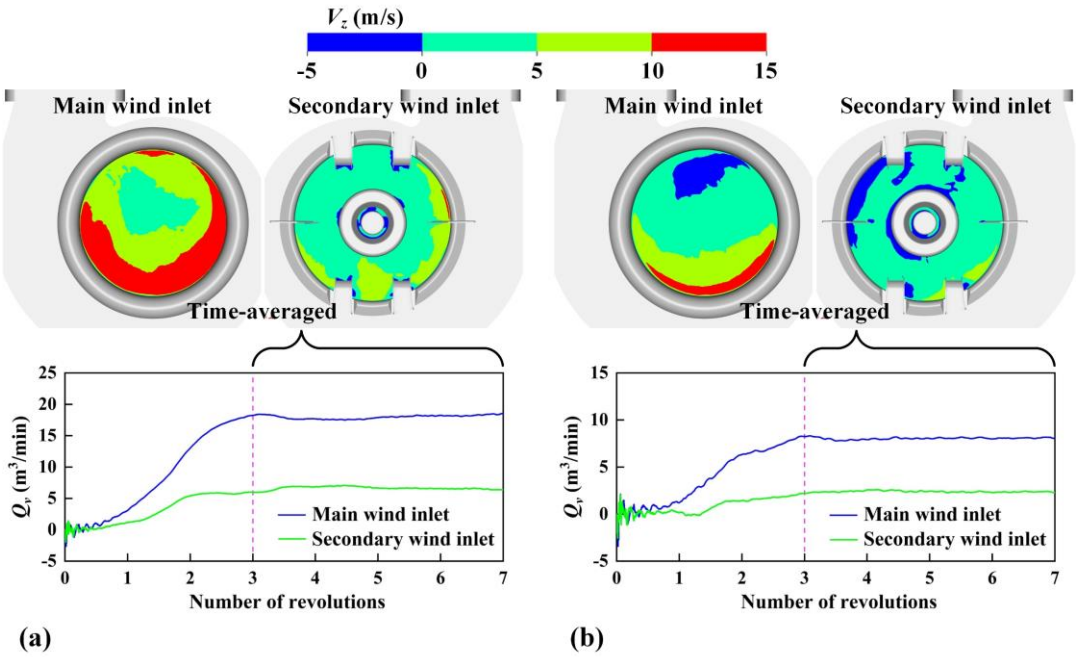

Fig. 12 Time-averaged *z*-velocity distribution and time history of the effective Q_v at the fan inlet: (a) Case 1 and (b) Case 2

results for the OASPLs at microphone observation points. The average OASPL absolute error of the four microphone observation points for Case 1 and Case 2 is 0.7 dBA, meaning that agreement is achieved in the simulations with relatively small errors, indicating that the computational model and method accurately predict fan noise. These errors can be explained by the rotation speed fluctuations and corrugated tubes in the experiment; the effects of these on the acoustic characteristics are not accurately modeled in the simulation. In summary, the computational strategy of CAA based on the LBM proposed in this paper can accurately compute the full three-dimensional flow and acoustic field of a double-suction multiblade centrifugal fan under two typical operating conditions in an actual application scenario. Reliable simulation results can be used to gain a detailed understanding of a fan's aerodynamic and aeroacoustic characteristics.

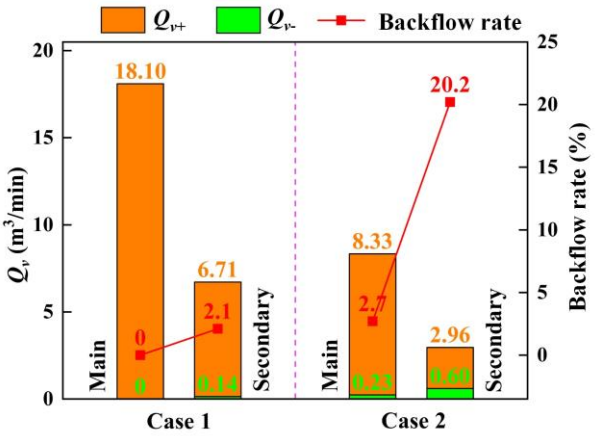

Fig. 13 Backflow rate and time-averaged Q_v at the fan inlet

3.2 Asymmetric Wind Intake at the Fan Inlet

Figure 12 presents the time-averaged *z*-velocity (V_z) distribution and the time history of the effective Q_v ($Q_{v+} - Q_{v-}$) at the fan inlet. Here, the volume flow rate Q_{v+} indicates a positive value of V_z when the airflow enters the volute, whereas Q_{v-} indicates a negative value of V_z when a backflow flow is directed toward the outside of the volute. The backflow rate is expressed as $(Q_{v-}/Q_{v+}) \times 100\%$ (Fig. 13). Similarly, the effective Q_v at the fan inlet converges after three impeller revolutions, and the transient data for the last four revolutions are averaged. In Case 2, a notable backflow phenomenon clearly occurs at both the main and secondary wind inlets. The backflow rates are 2.7% and 20.2%, respectively. Unlike Case 2, the main wind inlet in Case 1 has no backflow, and the secondary wind inlet has a small amount of backflow due to the influence of the motor bracket, with a backflow rate of 2.1%. This observed disparity in backflow rates can be attributed to the distinct flow characteristics exhibited by the volute.

Furthermore, on the basis of the effective flow rate, the main and secondary wind inlets of Case 1 account for approximately 73% and 27% of the Q_v at the fan inlet, respectively. The main and secondary wind inlets of Case 2 account for approximately 77% and 23% of the Q_v at the fan inlet, respectively. Therefore, in the application scenarios described in this paper, more than 70% of the airflow enters the volute from the main wind inlet. This is because the range hood obtains the intake wind from the back, most of the airflow through the smoke collection channel enters the volute at a relatively high flow velocity from the main wind inlet, and a small part of the airflow bypasses the gap between the volute and the upper shell to enter the volute from the secondary wind inlet at a

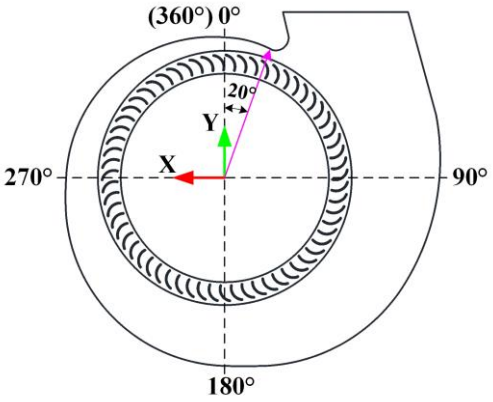

Fig. 14 Circumferential angle of the fan

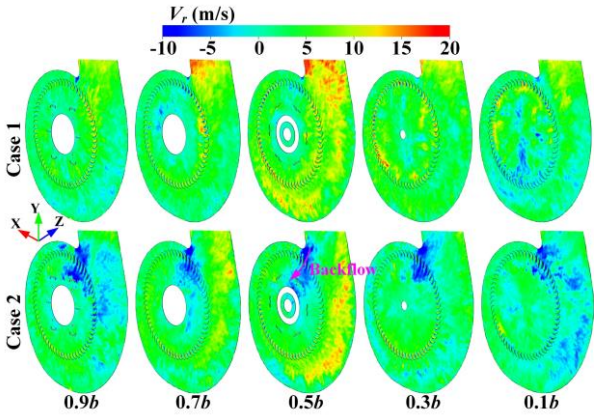

Fig. 16 Instantaneous radial velocity distributions on the different blade height sections

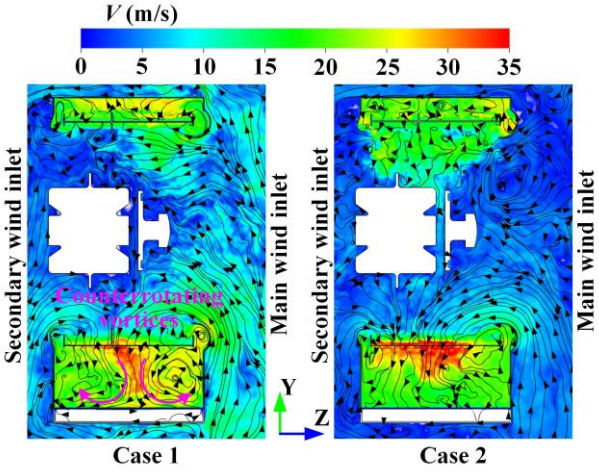

Fig. 15 Instantaneous velocity with the streamline distribution in the YOZ section

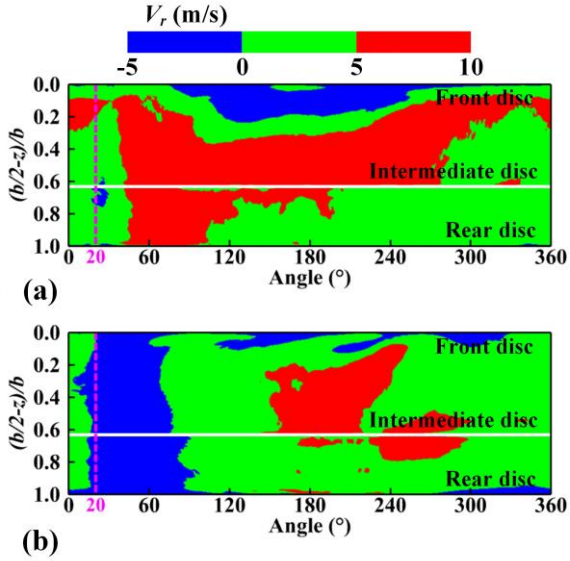

Fig. 17 Time-averaged radial velocity distribution at the entrance of the impeller: (a) Case 1 and (b) Case 2

relatively low flow velocity (Fig. 1). This asymmetric wind intake phenomenon at the fan inlet is essential for revealing the fan's true aerodynamic and aeroacoustic characteristics.

3.3 Flow Pattern Inside the Volute

The asymmetric wind intake conditions from the main and secondary wind inlets of the double-suction multiblade centrifugal fan lead to the formation of an asymmetric flow pattern inside the volute along the axial direction. This section analyzes the relevant flow characteristics. Figure 14 depicts a circumferential coordinate system in which the angle increases clockwise and 0° is in the positive direction of the Y-axis. The initial declination of the volute tongue is 20°.

Figure 15 illustrates the instantaneous velocity with the streamline distribution on the YOZ section. The airflow enters the interior of the volute along an axial direction and then tends to enter the blade channel along the radial direction near the intermediate disc. Vortices in the gap between the impeller and the inlet nozzle are the main source of gap leakage. In addition, Case 1 has a stronger swirling flow in the volute flow channel at the 180° position, forming a pair of counterrotating vortices. This is related to the large wind intake capacity of the main wind inlet. In Case 2, the flow pattern in the volute flow channel becomes more disordered at the 0° position because the impeller backflow phenomenon occurs in the vicinity of the volute tongue.

The flow velocity is decomposed into a radial velocity (V_r) along the radial direction of the impeller, which is defined as positive when the impeller diameter increases. Figure 16 depicts the V_r distributions for different blade height sections. For both cases, V_r is greater for the 50% blade height (0.5b) section, clearly showing the asymmetric flow pattern inside the volute along the axial direction. More importantly, Case 2, with a smaller volume flow rate, presented greater impeller backflow in the blade channel near the volute tongue, consistent with the phenomenon observed by Liu et al. (2021). This can be attributed to the finding that the fan operates at a lower volume flow rate with a high outlet static pressure. The adverse pressure gradient near the volute tongue drives the airflow entering the blade channel in the reverse direction.

Figure 17 shows the time-averaged V_r distribution at the impeller's entrance. The positive value of V_r represents

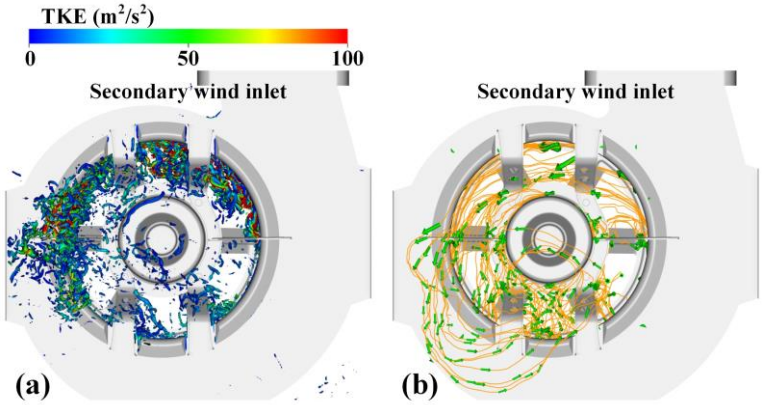

Fig. 18 Backflow at the secondary wind inlet for Case 2: (a) Iso-surface of Q = 1.0 × 10^6 s^{-2}, colored with the contour of the turbulence kinetic energy, and (b) streamline

the effective throughflow zone in the blade channel. The impeller is divided into front and rear segments, with the intermediate disc as the interface. The larger throughflow volume occurred mainly in the front segment of the impeller. However, for Case 1, the backflow occurred in the range of 0~0.2b, spanning the blade channel approximately 90°~270°. This is associated with a pair of counterrotating vortices that formed near the 180° position of the volute flow channel shown in Fig. 15. Additionally, in Case 2, the backflow occurred over the entire range of blade heights near the volute tongue, spanning the blade channel at approximately 20°~75° and 20°~90° in the front and rear segments of the impeller, respectively. This difference in backflow between the impeller's front and rear segments is also an important reason for the difference in cross-impeller flow in the axial direction.

The cross-impeller flow originates from the impeller backflow near the volute tongue. In Case 2, the distribution region of backflow on different blade height sections gradually increases from the impeller's front segment to its rear segment (Fig. 16). This can be explained by the three-dimensional flow characteristics of the cross-impeller flow; that is, the reverse flow near the volute tongue penetrating the blade channel flows a certain distance along the direction of impeller rotation and then returns to the blade channel from the impeller inlet. In the axial direction, the cross-impeller flow gradually moves toward the rear disc as it traverses the impeller along the direction of impeller rotation until the airflow re-enters the blade channel and shifts to the rear disc of the impeller. Part of the airflow even leaks to the outside of the volute from the inlet nozzle. It is most pronounced at the secondary wind inlet of Case 2; Fig. 18 depicts the iso-surface map (Q = 1.0 × 10^6 s^{-2}) colored by turbulence kinetic energy (TKE) and the streamline. The backflow strikes the inlet nozzle near 270° and re-enters the volute with the main flow near 180°.

In summary, Case 2, which operates at a lower volume flow rate, exhibits greater impeller backflow near the volute tongue than Case 1, operating at a higher volume flow rate. The synergy of the asymmetric wind intake condition and the cross-impeller flow caused by the impeller backflow results in airflow leakage to the outside of the volute, and the backflow strikes the inlet nozzle near

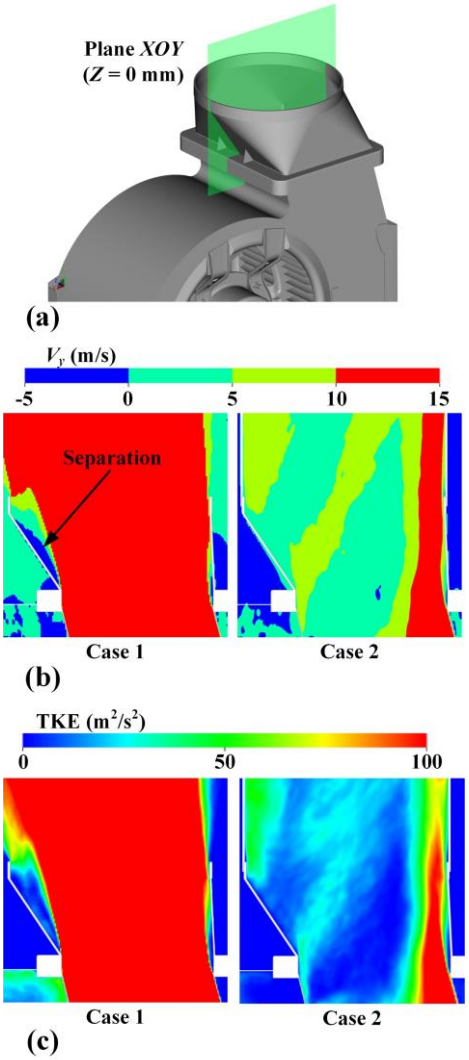

Fig. 19 Time-averaged flow characteristics inside the outlet collector: (a) Diagram of the plane XOY (Z = 0 m) position inside the outlet collector, (b) *y*-velocity, and (c) turbulence kinetic energy

270°. To improve the aerodynamic and aeroacoustic characteristics of the fan, this area requires particular attention. Figure 19 shows the time-averaged distributions

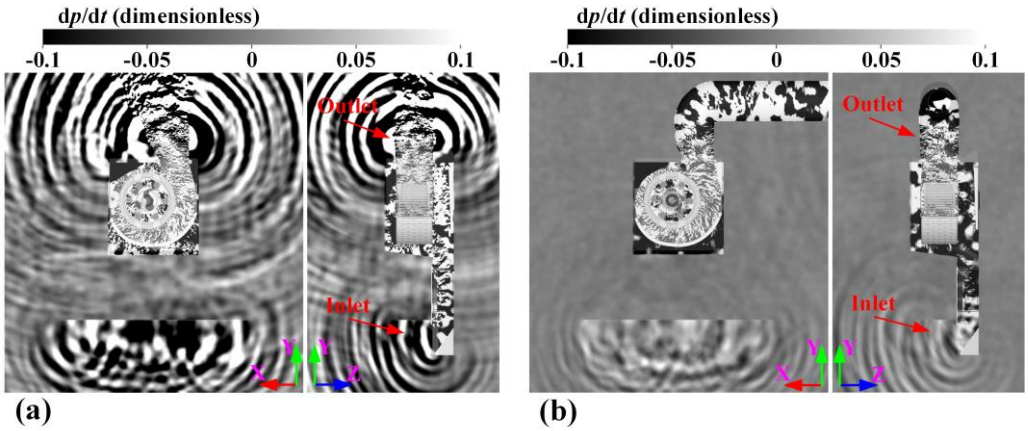

Fig. 20 Instantaneous acoustic field shown by the contour of the time derivative of pressure: (a) Case 1 and (b) Case 2

of the *y*-velocity (V_y) and TKE on the XOY plane (Z = 0 m) inside the outlet collector. Compared with Case 2, Case 1 has greater flow separation, which creates a flow separation vortex, leading to blockage of the outlet collector. Furthermore, Case 1 results in a higher TKE, which is a significant parameter associated with dipole and quadrupole noise. In general, a higher TKE means more noise. The optimal design of the outlet collector structure will also help improve the fan's aerodynamic and aeroacoustic characteristics.

3.4 Noise Characteristics of the Range Hood

The dilatation field represents instantaneous acoustic perturbations. The time derivative of pressure (d*p*/d*t*) is a suitable quantity for visualizing the acoustic field, as it is proportional to the dilatation field. Additionally, d*p*/d*t* tends to amplify high-frequency fluctuations in pressure, which are indicative of acoustic fluctuations (Damiano et al., 2019). Figure 20 presents the instantaneous distributions of the acoustic field on planes XOY (Z = 0 mm) and YOZ (X = –105 mm), represented by d*p*/d*t*. The XOY plane is located at the 0.5*b* section, and the YOZ plane passes through the center of the circular outlet of the outlet collector.

In Case 1, the acoustic waves around the range hood can be observed as multiple concentric patterns with unequal spacing at the inlet and outlet. This distribution indicates that the acoustic waves radiate to the far-field at multiple frequencies, mainly through the range hood's inlet and outlet. Interference is observed between the upward-directed acoustic wave from the inlet region and the downward-directed acoustic wave from the outlet region. The vortex-induced pressure changes dramatically in the outlet region, thereby strengthening the acoustic energy. The acoustic waves are diffracted in the inlet region because of the smoke barrier. Furthermore, the acoustic waves' interference in the inlet region is displayed on the YOZ plane. In Case 2, the high value of d*p*/d*t* is constrained inside the smoke tube, resulting in significant differences between the two cases with respect to the acoustic field characteristics in the outlet region. The acoustic waves propagating to the far field mainly originate from the inlet region and exhibit similar acoustic field characteristics to those in Case 1 but with lower intensity.

The spectrum analysis was performed at the microphone observation points to evaluate the overall noise characteristics of the range hood. Figure 21 demonstrates the SPL spectra of the microphone observation points. The SPL spectrum is displayed on a two-dimensional (2D) colormap, with the SPL spectra for only four microphone observation points (MIC-Front, MIC-Rear, MIC-Left, and MIC-Right) shown as curves. In both cases, the SPL spectrum at the front of the range hood is greater than that at its rear. However, no significant single peak was observed, indicating that there was no obvious BPF noise. This may be attributed to the finding that BPF noise is not prominent because of the large number of blades and the use of the full geometric model of the range hood, which includes sound absorption materials in the simulation. Interference and absorption occur in the range hood's complex flow channel as acoustic waves propagate through it. Similar results were reported by Hu et al. (2023). The experimental data shown in Figs. 10 and 11, with a frequency resolution of 1.0 Hz, also exhibit the same phenomenon. Even without a noticeable peak, the SPL spectrum displays crests and troughs, which can be explained by the sound pressure phase superposition during propagation.

In Case 1, SPL values above 40 dBA at the front of the range hood are mostly distributed within 0~2250 Hz, and those at its rear are mostly distributed within 0~600 Hz. SPL values above 30 dBA extend to 3500 Hz at the front of the range hood and to 2000 Hz at its rear. In Case 2, SPL values above 40 dBA are sporadically distributed at the peaks within 0~500 Hz at the front of the range hood. SPL values above 30 dBA are mostly distributed within 0~2900 Hz at the front of the range hood and 0~1300 Hz at its rear. Consequently, the range hood's acoustic source is mainly broadband noise, with noise at its front primarily concentrated at low and middle frequencies and noise at its rear concentrated mainly at low frequencies. Thus far, the noise characteristics of the actual application scenario of a double-suction multiblade centrifugal fan are different from the significant discrete noise exhibited by a single centrifugal fan. This difference

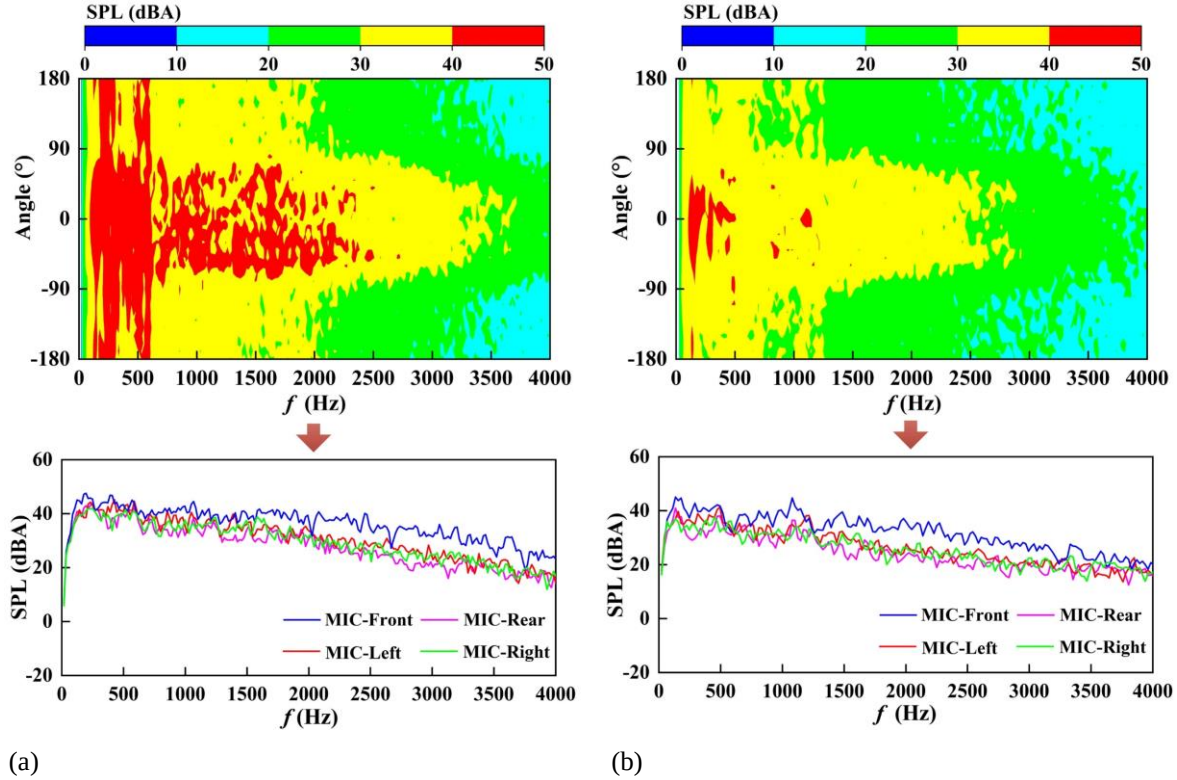

Fig. 21 Spectrum of the SPL at the microphone observation points: (a) Case 1 and (b) Case 2

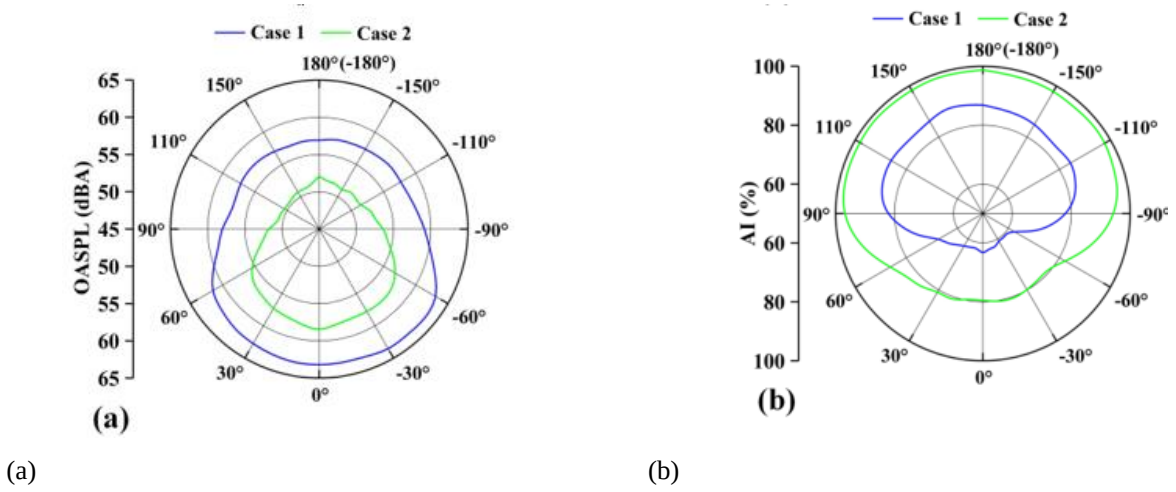

Fig. 22 Acoustic radiation directivity of the range hood: (a) Overall sound pressure level and (b) articulation index

presents a serious challenge to reducing the overall noise of the range hood by decreasing the SPL at the specific frequencies where the noise peaks are more pronounced.

Figure 22(a) presents the acoustic radiation directivity of the range hood in a polar plot of the OASPLs at all microphone monitoring points. In Case 1 and Case 2, the OASPL at the front of the range hood is, on average, 5.0 dBA and 5.5 dBA higher than that at its rear, respectively. This is because more acoustic radiation is transmitted outward from the inlet at the front of the range hood. Moreover, the OASPL of Case 1 is approximately 4.5~6.5 dBA higher than that of Case 2 for each microphone observation point. The acoustic radiation directivities of the two cases are more similar, but the propagation characteristics of a dipole source are not very evident. Figure 22(b) shows the articulation index (AI) for each orientation. The AI is a noise metric representing the percentage of normal speech understood in the presence of noise at this SPL (Kryter, 1962). The index is in the range of 0% < AI < 100%, where a higher value indicates better speech intelligibility. In Case 1 and Case 2, the AI at the rear of the range hood is, on average, 20% and 15% higher than the AI at its front, respectively. Additionally, for each orientation, the AI of Case 2 is approximately 10%~20% higher than that of Case 1.

3.5 Acoustic Source Localization

Revealing the range hood's noise characteristics is not enough to guide the design of passive noise reduction. Further investigation of the acoustic source characteristics

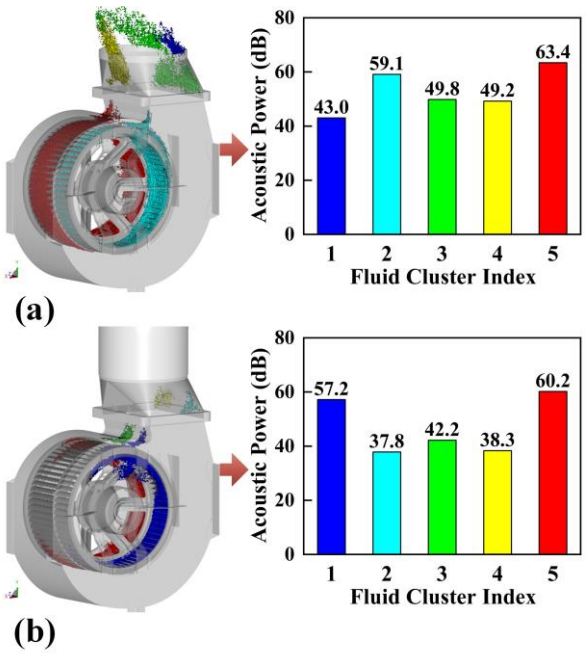

Fig. 23 Clustering of the acoustic power at the 315 Hz 1/3 octave frequency band: (a) Case 1 and (b) Case 2

is essential. In this study, the acoustic source was analyzed qualitatively and quantitatively on the basis of vortex sound theory (Powell, 1964). Each source was quantified according to its acoustic power. Fluid clusters were employed to visualize the volume acoustic sources of the range hood. Acoustic sources within the same area were grouped to identify regions with higher noise levels. More information can be found in Mann et al. (2015).

Although the results for all frequency bands could help assign the main acoustic sources to different frequencies, describing only a single frequency as an example is sufficient to guide the design of passive noise reduction. Figure 23 shows the acoustic power clustering for the 315 Hz 1/3 octave frequency band. To show regions of high noise levels, we consider only measurement cells for which the acoustic power exceeds a certain threshold so that, in both cases, there are five clusters of interest. In addition, the noise level is described by evaluating the overall acoustic power radiated by each cluster. The decibel values are calculated on the basis of the acoustic energy. As expected, in both cases, most volume acoustic sources are located within the centrifugal fan. The region with the maximum volume acoustic source intensity is at the front segment of the impeller, followed by its rear segment. There is a considerable discrepancy between the two cases with respect to the volume acoustic sources in the vicinity of 270°. This may be attributed to the finding that the cross-impeller flow in Case 2 improves the flow at the impeller inlet and mitigates the flow separation in the blade channel. The volume acoustic sources of the blade channel and wake are related to the airflow separation at the leading edge of the blade and the vortex shedding in the blade wake region. A high-volume acoustic source intensity is also observed near the volute tongue and inside the outlet collector. The volume acoustic sources inside the outlet collector of Case 1 have a larger distribution range and a higher noise level, which are associated with flow phenomena in this area (Fig. 19).

The volume acoustic source generated by turbulent fluctuations has a broadband spectrum and is an important broadband noise source. Another important tonal noise source originates from the surface acoustic source generated by wall pressure fluctuations. Although the spectrum of the microphone observation points did not exhibit significant tonal noise related to the BPF, revealing the surface acoustic source's location and intensity can still help guide the design of low-noise structures for the fan. Figure 24 shows the SPL distribution on the volute surface at the 315 Hz 1/3 octave frequency band, which is involved in the generation of dipole noise. For the volute's external surface in Case 1, the highest surface acoustic source intensity is at the inlet nozzle on the side of the

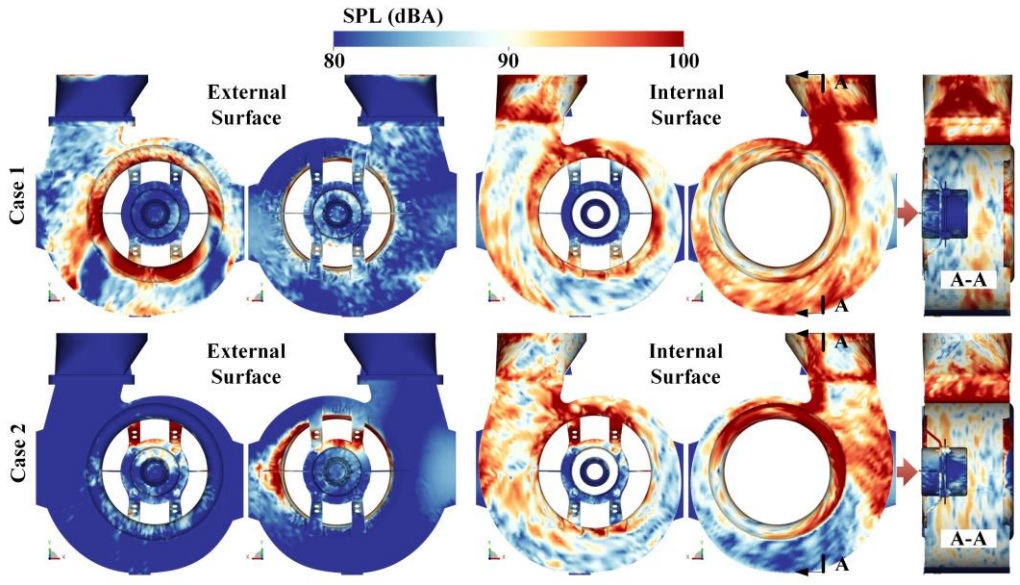

Fig. 24 Sound pressure level distribution on the volute surface at 315 Hz in the 1/3 octave frequency band

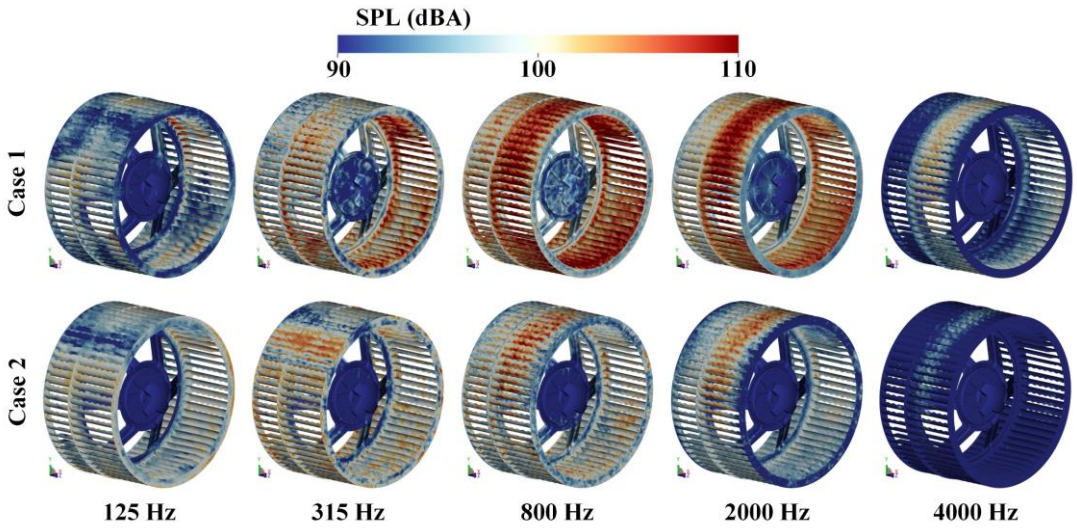

Fig. 25 Sound pressure level distributions on the impeller surface at different frequencies

main wind inlet. In Case 2, it is near 270° of the inlet nozzle on the side of the secondary wind inlet. The former could be associated with the strong turbulence observed at the main wind inlet under the operating conditions of a relatively high volume flow rate. The latter is related to the backflow from the secondary wind inlet striking the wall. For the volute's internal surface, the highest surface acoustic source intensity is located near the volute tongue and the gap between the impeller and the inlet nozzle. The strong interaction between the blade wake and the volute tongue is the main reason for the acoustic source in the volute tongue region. The acoustic source in the gap between the impeller and the inlet nozzle is related to the vortex between them, which interacts with the main flow and the wall. The surface acoustic source intensity is greater at the outlet collector in Case 1 and at the motor bracket in Case 2. The former is associated with the internal flow characteristics depicted in Fig. 19, whereas the latter is associated with the backflow from the secondary wind inlet.

Figure 25 shows the SPL distribution on the impeller surface at different frequencies in the 1/3 octave frequency band. As the frequency increases, the high surface acoustic source intensity gradually becomes concentrated in the front segment of the impeller. The surface acoustic source intensity of Case 1 is higher than that of Case 2 in all frequency bands. This phenomenon can be observed more directly in Fig. 26 from the pressure fluctuation on the impeller surface represented by the standard deviation of pressure ($StDev = \sqrt{\frac{1}{N}\sum_{i=1}^{N}(p_i - \bar{p})^2}$). In Case 1, the strong pressure fluctuations are located not only on the pressure surface of the blade near the front disc but also on the suction surface of the blade, which is distributed over almost the entire blade height. However, in Case 2, the strong pressure fluctuations are located only on the suction surface of the blade near the intermediate disc and close to the trailing edges. This difference in pressure fluctuations on the blade surface is closely related to the pattern of flow separation in the blade channel. Concurrently, the distribution characteristics of the pressure fluctuations are also reflected in the distribution characteristics of the surface acoustic source on the impeller.

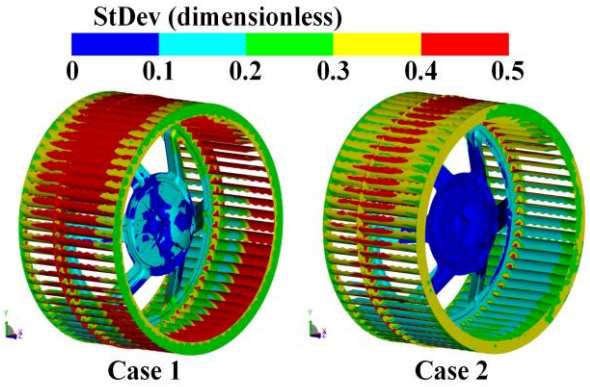

Fig. 26 Pressure fluctuation distribution on the impeller surface

Consistent with the results of most previous studies, the acoustic sources are identified in the impeller region, the volute tongue, and the gap between the impeller and the inlet nozzle. However, this study considered the actual application scenario of a double-suction multiblade centrifugal fan, not only adopting a full-scale geometric model of the range hood but also including sound absorption material. We were therefore able to identify two other significant acoustic sources located in the outlet collector and inlet nozzle regions. Designers are consistently seeking to enhance product performance through incremental structural modifications, and these two acoustic sources will undoubtedly serve as a source of inspiration. Optimizing complex structures such as impellers and volutes within the constraints of limited space dimensions is challenging, and the performance benefits obtained under different operating conditions are inconsistent. In contrast, the outlet collector and inlet nozzle have simple structures and allow for product upgrades at low cost.

4. CONCLUSION

This study involved a detailed numerical investigation of the aerodynamic and aeroacoustic characteristics of a double-suction multiblade centrifugal fan under different operating conditions. The actual application scenario of the fan is a domestic appliance range hood. The direct CAA method based on the LBM was used to solve the full three-dimensional flow and acoustic field simultaneously. The numerical simulation's accuracy was verified using experimentally measured data from the performance test bench and the semianechoic chamber. The flow patterns were analyzed, and the locations and intensities of the main noise sources were identified. The following conclusions were obtained:

(1) The full three-dimensional flow and acoustic field of a double-suction multiblade centrifugal fan in an actual application scenario were successfully predicted using direct CAA based on the LBM. The relative error of volume flow rate Q_v is less than 2.0%, and the absolute error of the total pressure efficiency η_t is less than 4.0%. The absolute error of the averaged OASPL for the four microphone observation points is 0.7 dBA. Meanwhile, the spectrums of the simulated and measured values exhibit high agreement throughout the frequency range of interest.

(2) In the actual application scenarios described in this paper, more than 70% of the airflow enters the volute from the main wind inlet. This asymmetric wind intake condition leads to an asymmetric flow pattern inside the volute. In Case 1, significant flow separation is observed in the outlet collector, causing a flow separation vortex and leading to blockage of the outlet collector. In Case 2, an adverse pressure gradient near the volute tongue causes the airflow to enter the blade channel in the opposite direction, leading to the impeller backflow phenomenon while causing cross-impeller flow. The synergy of the asymmetric wind intake condition and the cross-impeller flow causes airflow leakage from the secondary wind inlet to the outside of the volute and continuously strikes the inlet nozzle near 270°.

(3) The acoustic waves radiate to the far field at multiple frequencies, mainly through the range hood's inlet and outlet. The two cases have relatively similar acoustic radiation directivities, but the propagation characteristics of a dipole source are not very obvious and the tonal noise associated with the blade passage frequency (BPF) is not significant. In addition to the acoustic sources identified in the regions of the impeller, volute tongue, and the gap between the impeller and the inlet nozzle, two other significant acoustic sources are located in the outlet collector and inlet nozzle regions.

The high computational accuracy and efficiency of the direct CAA method based on LBM indicate its significant potential for application in engineering and it represents a promising alternative to traditional methods. The acoustic sources located in the region of the outlet collector and the inlet nozzle are associated with the corresponding flow phenomena. These flow phenomena must be addressed to optimize the fan's aerodynamic and aeroacoustic performance. This is seen as the future scope of work.

ACKNOWLEDGEMENTS

This work was supported by the National Natural Science Foundation of China (grant nos. 12372288 and U23A2069).

CONFLICT OF INTEREST

The authors declare that they have no known competing financial interests or personal relationships that could have appeared to influence the work reported in this paper.

AUTHORS CONTRIBUTION

Hao Zhang: Conceptualization; Formal analysis; Methodology; Software; Validation; Visualization; Writing - original draft. **Jinwen Yang**: Conceptualization; Data curation; Investigation; Methodology; Validation. **Shaoguang Zhang**: Conceptualization; Data curation; Investigation. **Bin Li**: Conceptualization; Supervision. **Jun Wei**: Conceptualization; Investigation. **Yufei Zhang**: Conceptualization; Methodology; Supervision; Writing - review & editing.

REFERENCES

Bai, M., Liu, Z., Ling, Y., & Tan, H. (2024). Effect of impeller structure on aerodynamic performance and noise reduction of a small multi-blade centrifugal fan. *Science and Technology for the Built Environment*, *30(6)*, 563–578. https://doi.org/10.1080/23744731.2024.2357526

Baloni, B. D., Pathak, Y., & Channiwala, S. A. (2015). Centrifugal blower volute optimization based on Taguchi method. *Computers and Fluids*, *112*, 72–78. https://doi.org/10.1016/j.compfluid.2015.02.007

Basner, M., Brink, M., Bristow, A., de Kluizenaar, Y., Finegold, L., Hong, J., Janssen, S. A., Klaeboe, R., Leroux, T., Liebl, A., Matsui, T., Schwela, D., Sliwinska-Kowalska, M., & Sörqvist, P. (2015). ICBEN review of research on the biological effects of noise 2011-2014. *Noise Health*, *17(75)*, 57–82. https://doi.org/10.4103/1463-1741.153373

Carlos, P. A., Thomas, L., Marlène, S., Stéphane, M., & Florent, D. (2019). Large Eddy simulation of a scale-model turbofan for fan noise source diagnostic. *Journal of Sound and Vibration*, *445*, 64–76. https://doi.org/10.1016/j.jsv.2019.01.005

Casalino, D., Velden, W., & Romani, G. (2019). Community noise of urban air transportation vehicles. *AIAA 2019-1834. AIAA Scitech 2019 Forum*. San Diego, California. https://doi.org/10.2514/6.2019-1834

Chen, H., Kandasamy, S., Orszag, S., Shock, R., Succi, S., & Yakhot, Y. (2003). Extended Boltzmann kinetic

equation for turbulent flows. *Science*, *301*, 633–636. https://doi.org/10.1126/science.108504

Chen, J., He, Y., Gui, L., Wang, C., Chen, L., & Li, Y. (2018). Aerodynamic noise prediction of a centrifugal fan considering the volute effect using IBEM. *Applied Acoustics*, *132*, 182−190. https://doi.org/10.1016/j.apacoust.2017.10.015

Chen, S., & Doolen, G. D. (1998). Lattice Boltzmann method for fluid flows. *Annual Review of Fluid Mechanics*, *30(1)*, 329–364. https://doi.org/10.1146/annurev.fluid.30.1.329

Damiano, C., Francesco, A., Ignacio, G. M., & Daniele, R. (2019). Aeroacoustic study of a wavy stator leading edge in a realistic fan/OGV stage. *Journal of Sound and Vibration*, *442*, 138–154. https://doi.org/10.1016/j.jsv.2018.10.057

Freed, D. M. (1998). Lattice-Boltzmann method for macroscopic porous media modeling. *International Journal of Modern Physics C*, *9(8)*, 1491–1503. https://doi.org/10.1142/S0129183198001357

Gholamian, M., Rao, G., & Bhramara, P. (2013). Numerical investigation on effect of inlet nozzle size on efficiency and flow pattern in squirrel cage fans. *Proceedings of the Institution of Mechanical Engineers, Part A: Journal of Power and Energy*, *227(8)*, 896–907. https://doi.org/10.1177/0957650913504566

Gianluca, R., & Damiano, C. (2019). Rotorcraft blade-vortex interaction noise prediction using the Lattice-Boltzmann method. *Aerospace Science and Technology*, *88*, 147–157. https://doi.org/10.1016/j.ast.2019.03.029

Gianluca, R., Damiano, C., & Velden, W. (2021). Numerical analysis of airfoil trailing-edge noise for straight and serrated edges at incidence. *AIAA Journal*, *59(7)*, 2558–2577. https://doi.org/10.2514/1.J059457

Guillaume, B., Franck, P., & David, F. (2009). *Properties of the lattice Boltzmann method for acoustics. AIAA 2009-3395.* 15th AIAA/CEAS Aeroacoustics Conference (30th AIAA Aeroacoustics Conference). Miami, Florida. https://doi.org/10.2514/6.2009-3395

Hu, S., Wu, J., Hu, X., Chen, P., & Zhang, L. (2023). Study on main noise sources and partition contribution of a multi-blade centrifugal fan in a range hood. *Fluid Machinery*, *51(12)*, 64–70. https://doi.org/10.3969/j.issn.1005-0329.2023.12.010

Kazuya, K., Kazutoyo, Y., & Masato, F. (2020). Aeroacoustic simulation of broadband sound generated from low-Mach-number flows using a lattice Boltzmann method. *Journal of Sound and Vibration*, *467*, 115044. https://doi.org/10.1016/j.jsv.2019.115044

Keyur, P., & Prajesh, M. (2013). Performance analysis and optimization of centrifugal fan. *International Journal of Emerging Trends in Engineering and Development*, *3(2)*, 261–270. https://www.researchgate.net/publication/286354454

Kim, J. S., Jeong, U. C., Kim, D. W., Han, S. Y., & Oh, J. E. (2015). Optimization of sirocco fan blade to reduce noise of air purifier using a metamodel and evolutionary algorithm. *Applied Acoustics*, *89*, 254–266. https://doi.org/10.1016/j.apacoust.2014.10.005

Kryter, K. D. (1962). Methods for the calculation and use of the articulation index. *The Journal of the Acoustical Society of America*, *34(11)*, 1689–1697. https://doi.org/10.1121/1.1909094

Liu, H., Jiang, B., Wang, J., Yang, X., & Xiao, Q. (2021). Numerical and experimental investigations on non-axisymmetric D-type inlet nozzle for a squirrel-cage fan. *Engineering Applications of Computational Fluid Mechanics*, *15(1)*, 363–376. https://doi.org/10.1080/19942060.2021.1883115

Lu, H., Xiao, Y., Liu, Z., Yuan, Y., Zhou, P., & Yang, G. (2023). Investigation on accuracy of numerical simulation of aerodynamic noise of single-stage axial fan. *Physics of Fluids*, *35(11)*, 115136. https://doi.org/10.1063/5.0174731

Mann, A., Pérot, F., Meskine, M., & Kim, M. S. (2015). *Designing quieter HVAC systems coupling LBM and flow-induced noise source identification methods.* 10th FKFS-Conference, Progress in Vehicle Aerodynamics and Thermal Management. Stuttgart, Germany. https://www.researchgate.net/publication/282442139

Melanie, P., Bruno, B. C., Vincent, L. G., Vincent, V., & Franck, P. (2014). *Direct aeroacoustics simulation of automotive engine cooling fan system: effect of upstream geometry on broadband noise.* AIAA 2014-2455. 20th AIAA/CEAS Aeroacoustics Conference. Atlanta, United States. https://doi.org/10.2514/6.2014-2455

Michael, C., Leon, B., Mehdi, R. K., Ehab, F., & Benedikt, K. (2021). Comparison of Boeing 777 airframe noise flight test data with numerical simulations. *AIAA 2021-2162. AIAA Aviation 2021 Forum*. Virtual Event. https://doi.org/10.2514/6.2021-2162

Moreau, S. (2022). The third golden age of aeroacoustics. *Physics of Fluids*, *34(3)*, 031301. https://doi.org/10.1063/5.0084060

Powell, A. (1964). Theory of vortex sound. *The Journal of the Acoustical Society of America*, *36(1)*, 177–195. https://doi.org/10.1121/1.1918931

Qian, Y. H., D'Humieres, D., & Lallemand, P. (1992). Lattice BGK models for Navier-Stokes equation. *Europhysics Letters*, *17(6)*, 479–484. https://doi.org/10.1209/0295-5075/17/6/001

Rebecca, S., & Martin, B. (2019). *Influence of the mesh size on the aerodynamic and aeroacoustics of a centrifugal fan using the Lattice Boltzmann Method.*

Proceedings of the 23rd International Congress on Acoustics: Integrating 4th EAA Euroregio 2019. Aachen, Germany. https://doi.org/10.18154/RWTH-CONV-239255

Rebecca, S., & Martin, B. (2020). Validation of the lattice Boltzmann method for simulation of aerodynamics and aeroacoustics in a centrifugal fan. *Acoustics*, *2(4)*, 735–752. https://doi.org/10.3390/acoustics2040040

Rui, X., Lin, L., Wang, J., Ye, X., He, H., Zhang, W., Zhu, Z. (2020). Experimental and comparative RANS/URANS investigations on the effect of radius of volute tongue on the aerodynamics and aeroacoustics of a sirocco fan. *Processes*, *8(11)*, 1442. https://doi.org/10.3390/pr8111442

Seo, S. J., Kim, K. Y., & Kang, S. H. (2003). Calculations of three-dimensional viscous flow in a multiblade centrifugal fan by modelling blade forces. *Proceedings of the Institution of Mechanical Engineers, Part A: Journal of Power and Energy*, *217(3)*, 287–297. https://doi.org/10.1243/095765003322066510

Simon, M., Denis, R., & Pierre, S. (2009). Comparison between lattice Boltzmann method and Navier–Stokes high order schemes for computational aeroacoustics. *Journal of Computational Physics*, *228(4)*, 1056−1070. https://doi.org/10.1016/j.jcp.2008.10.021

Stephan, M., Marlene, S., Stephane, M., Alain, B., & Anthony, G. (2013). *Tonal noise control of centrifugal fan using flow obstructions - experimental and numerical approaches*. AIAA 2013-2043. 19th AIAA/CEAS Aeroacoustics Conference. Berlin, Germany. https://doi.org/10.2514/6.2013-2043

Teruna, C., Manegar, F., Avallone, F., Ragni, D., Casalino, D., & Carolus, T. (2020). Noise reduction mechanisms of an open-cell metal-foam trailing edge. *Journal of Fluid Mechanics*, *898(A18)*. https://doi.org/doi:10.1017/jfm.2020.363

Tim, C., & Sanjiva, K. L. (2004). Computational aeroacoustics: progress on nonlinear problems of sound generation. *Progress in Aerospace Sciences*, *40(6)*, 345–416. https://doi.org/10.1016/j.paerosci.2004.09.001

Wang, K., Ju, Y., & Zhang, C. (2020). Experimental and numerical investigations on effect of blade trimming on aerodynamic performance of squirrel cage fan. *International Journal of Mechanical Sciences*, *177*, 105579. https://doi.org/10.1016/j.ijmecsci.2020.105579

Wei, Y., Wang, J., Xu, J., Wang, Z., Luo, J., Yang, H., Zhu, Z., & Zhang, W. (2022). Effects of inclined volute tongue structure on the internal complex flow and aerodynamic performance of the multi-blade centrifugal fan. *Journal of Applied Fluid Mechanics*, *15(3)*, 901–916. https://doi.org/10.47176/jafm.15.03.32847

Yang, X., Yang, Y., Jiang, B., Gao, X., Hu, T., Wang, J. (2024). Morphological effects of leading-edge sawtooth on the vortex evolution and acoustic characteristic of an ultra-thin centrifugal fan. *Physics of Fluids*, *36(6)*, 065103. https://doi.org/10.1063/5.0206927

Ye, J., Liu, W., Duan, P., Huang, X., Shao, J., & Zhang, Y. (2018). Investigation of the performance and flow behaviors of the multi-blade centrifugal fan based on the computer simulation technology. *Wireless Personal Communications*, *103*, 563–574. https://doi.org/10.1007/s11277-018-5461-7

Zhang, Y., Xiao, Y., Liu, R., & Chen, H. (2022). Aeroacoustic prediction based on large-eddy simulation and the Ffowcs Williams–Hawkings equation. *Advances in Aerodynamics*, *4(19)*, 1–18. https://doi.org/10.1186/s42774-022-00112-2

Zhou, W., Zhou, P., Xiang, C., Wang, Y., Mou, J., & Cui, J. (2023). A review of bionic structures in control of aerodynamic noise of centrifugal fans. *Energies*, *16(11)*, 4331. https://doi.org/10.3390/en16114331